

Research Article

A Finite Element Analysis Approach to Explain Sensitivity Degradation in Force Sensing Resistors Based on Conductive Polymer Composites

Arnaldo Matute ¹, Leonel Paredes-Madrid ², David Altuve ³ and Carlos A. Palacio ⁴

¹CIYT Group, Faculty of Engineering and Basic Science, Juan De Castellanos University Foundation, Tunja 150001, Colombia

²Faculty of Mechanics, Electronic and Biomedical Engineering, Universidad Antonio Nariño, Tunja 150001, Colombia

³Mechatronics Group, Simón Bolívar University, Caracas 1080, Venezuela

⁴GIFAM Group, Faculty of Sciences, Universidad Antonio Nariño, Tunja 150001, Colombia

Correspondence should be addressed to Arnaldo Matute; amatute@jdc.edu.co

Received 16 December 2021; Accepted 6 April 2022; Published 26 April 2022

Academic Editor: Salvatore Surdo

Copyright © 2022 Arnaldo Matute et al. This is an open access article distributed under the Creative Commons Attribution License, which permits unrestricted use, distribution, and reproduction in any medium, provided the original work is properly cited.

Force sensing resistors (FSR) based in conductive polymer composites (CPC) are a cost-effective alternative to load cells for force measurement. Nevertheless, their physical characteristics related to rheological features provoke some drawbacks such as hysteresis, drift, low repeatability, and sensitivity degradation (SD), which is a concerning issue when final application involves periodic loading. Although it is already known that SD is a voltage-related phenomenon and practical considerations to avoid it have been published, a more theoretical approach was yet missing. This study provides a set of finite element analysis (FEA) simplified models to shed light on the situations that favor degradation based in a time-dependent mechanical study considering rheological parameters and how they influence interparticle tunneling conduction. Also, a stationary electrostatic analysis with special scope in contact resistance and its influence in equipotential surfaces arousal. Simulation results show how the effect of contact resistance bends equipotential surfaces favoring conduction through time-increasing interparticle gaps, which is a direct consequence of the low Poisson ratio of considered polymers.

1. Introduction

Force sensing resistors (FSR) exhibit a notorious change in its electrical resistance when subjected to mechanical stress, what makes them a suitable device for electrical transduction of force or pressure. The brand to analyze in the present study, Flexiforce A201-X, offers a FSR product composed by two electrode terminals sandwiching a conductive polymer composite (CPC) with a disk-like geometry. Its electrical model is just a resistance whose ohmic value depends on the exerted force. Thus, with a simple conditioning circuit, they provide a low-cost reliable alternative to strain gauges and force cells, for measuring force or pressure [1].

CPC are composed of an electrically insulating matrix which contains conductive nanoparticles randomly dispersed in it. The electrical conduction relies on the quantum

tunneling (QT) phenomenon, where conduction between neighboring nanoparticles can be possible although a thin insulating film physically separates them [2]. This film behaves as a potential barrier that apparently hinders charge carriers to pass from a nanoparticle to its neighboring ones. Nevertheless, QT phenomenon considers that there are probabilities for some charge carriers to overcome the potential barrier, what establishes an electrical current between nanoparticles and throughout the thin film. Since the matrix is composed of polymer material, deformation is observed once the device is subjected to mechanical stress and the film between neighboring particles shrink due to deformation. Conduction probability increases when the separating thin film is reduced. Thus, the device allows a higher electrical current to flow because of the exertion of mechanical stress [3].

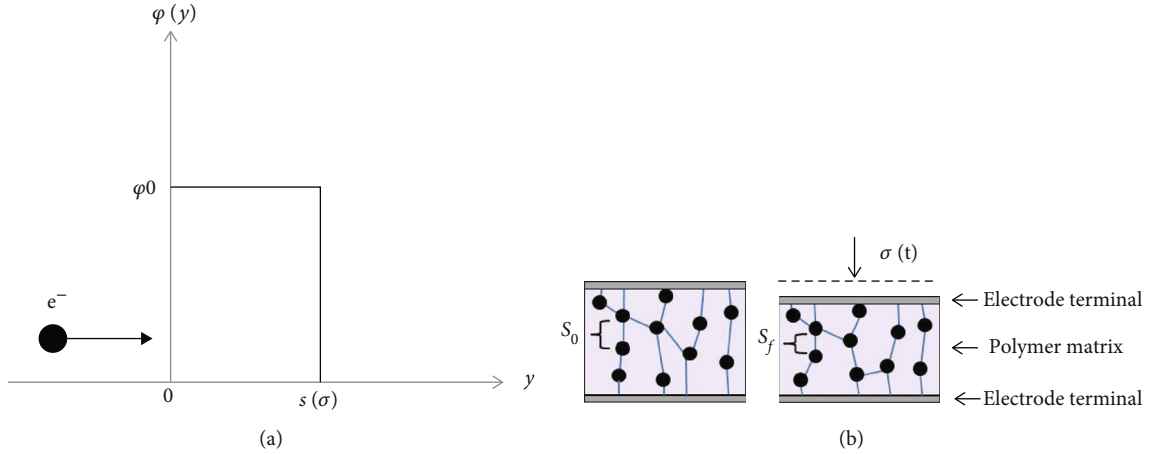


FIGURE 1: (a) Potential barrier scheme for tunneling conduction. (b) Sandwich-like FSR scheme where interparticle separation reduces when the device is subjected to mechanical stress $\sigma(t)$. Electric current flowing through the CPC in a multipath fashion. Blue lines depict the possible paths QT can occur through. Figure not to scale.

Simmons' proposal of a generalized formula for electrical conduction through thin insulating films [4] has been the basis for a series of contributions and studies made to broaden the knowledge of CPC devices. The effect of contact resistance [5], conduction area [6], random behavior [7], electrode alignment [8], rheological response [3], piezocapacitance [9–12], hysteresis [13–15], and also the proper considerations when conducting elements are nanotubes [16, 17] have been widely studied for a more accurate understanding. Therefore, more accurate models have been published, which allow to understand better the performance of FSR in several operating conditions.

FSRs, and generally CPCs, due to its conditions and the phenomena involved offer advantages regarding to cost, size, and weight. They are noninvasive devices suitable for plenty of applications in robotics [18, 19], industrial/biomedical instrumentation [1, 20], human-machine interfaces (HMI) [21, 22], catalysis [23], and energy storage [24, 25]. However, disadvantages such as hysteresis, low repeatability, and drift are undesirable characteristics of FSRs when compared, for instance, to force cells. Research has been conducted to propose techniques to lessen the reading errors provoked by phenomena such as hysteresis, repeatability [14], or drift [26]. Nevertheless, when the application involves exertion of periodic force patterns, sensitivity degradation (SD) remains an important concern to be addressed. Although practical considerations have been proposed to lessen the effect of SD, to the best of authors' knowledge a theoretical explanation is yet missing. This phenomenon hinders a precise calibration of sensor as applications demand nowadays. Hence, more precise modeling and studies are worth to be carried out to support experimental observations. Finite element analysis has been considered a pathway to build more accurate models relying on solving Dirichlet problems with the observed boundary conditions considering coupled electrical and mechanical phenomena. A simplified "four-particle-model" has been built in COMSOL Multiphysics® Modeling Software to simulate FSR operation of dynamic loading conditions that favors the observation of SD. Rheo-

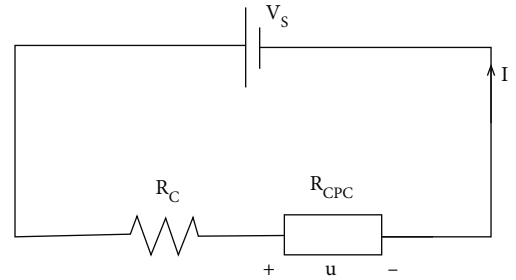


FIGURE 2: Electrical model for FSR based in CPC. R_C is the whole contact resistance the device provides. R_{CPC} is the tunneling resistance the CPC offers and V_s the sourcing voltage applied by the conditioning circuit. The voltage in R_{CPC} is u .

logic and electrostatic equations have been solved to serve as a basis for its physical explanation seen by periodic loading.

This paper is organized as follows: Section 2 will briefly discuss all considerations that drove authors to propose the most accurate model for commercial FSR based in CPC. Section 3 will address evidence of SD in dynamic loading conditions with special focus on its dependence on applied voltage. Section 4 explains the simplified "four-particle-model" to be executed in COMSOL Multiphysics® Modeling Software for the finite element analysis. Sections 5 and 6 address, respectively, the outcome of the mechanical dynamic and the electrical stationary studies with the scope in SD. Section 7 summarizes the conclusions and recommendations for future work.

2. Conduction Model of Force Sensing Resistors Manufactured from Conductive Polymer Composites

2.1. Comprehensive Model Embracing Rheological Phenomena. Any pressure exerted with a nonzero normal component on a FSR will provoke its deformation since its matrix is composed with low stiffness polymers. Inner conductive nanoparticles come closer together because of

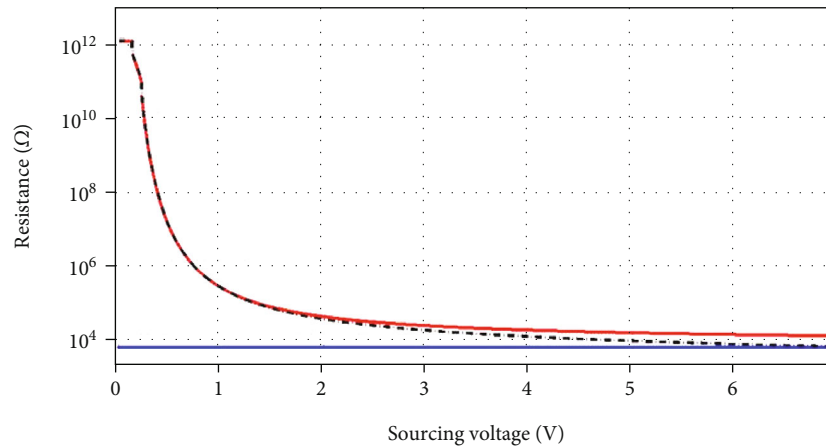


FIGURE 3: Resistances present in FSR for different sourcing voltages. Blue line represents the voltage-independent contact resistance R_c . R_{CPC} tunneling resistance in dashed black. Their sum, the total resistance, in red. For this graph, the following parameters were considered: $s_0 = 4.4$ nm, $\varphi_0 = 0.22$ eV, $k = 0.45$, $R_{par} = 2.27 \cdot 10^{-14}$ Ω , $R_c^0 = 1.197 \cdot 10^6$, $A = 5.81$ nm², and $M = 4.73$ MPa.

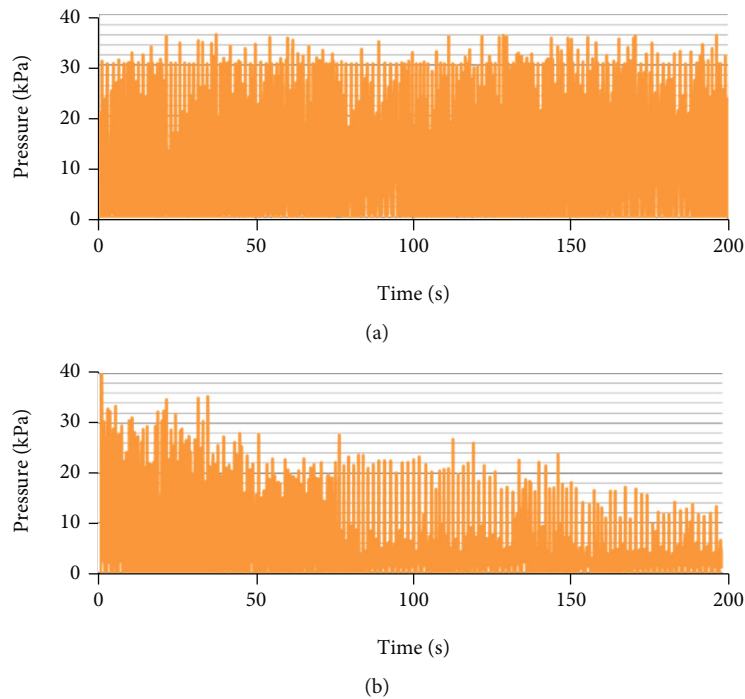
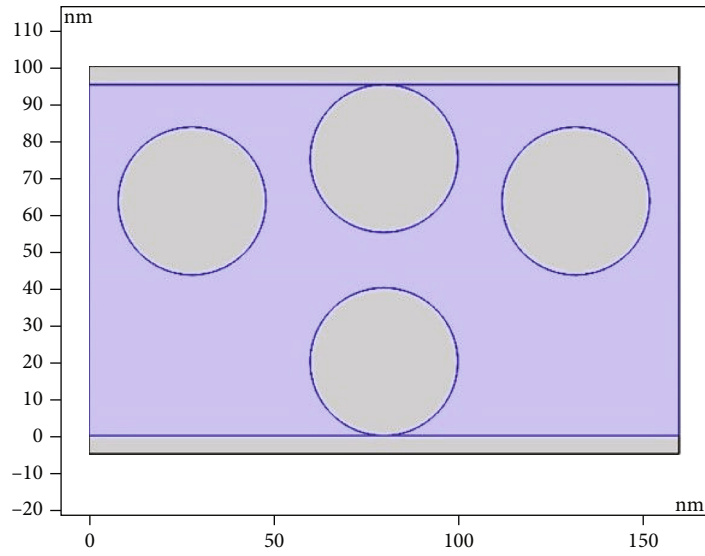


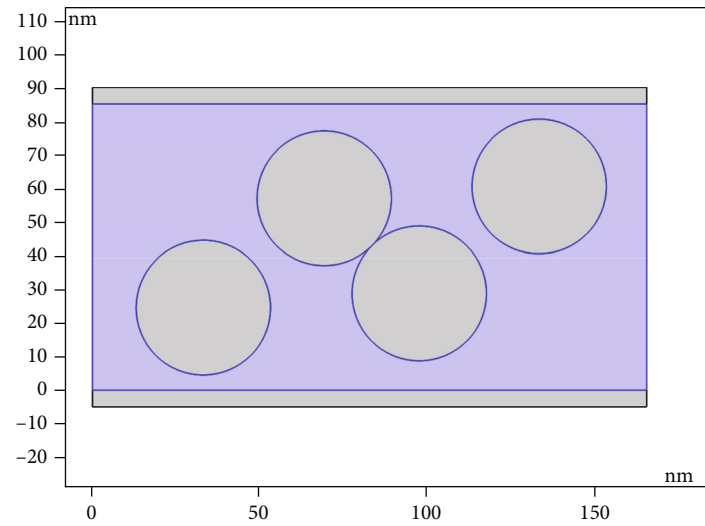
FIGURE 4: (a) Gait pattern where sensitivity of insole sensor does not degrade ($V_S = 1.27$ V). (b) Similar gait pattern where degradation is observed ($V_S = 9$ V) [28].

pressure, making the thin insulating film shrink in the direction of the exerted force and expands in the perpendicular direction. The thinner the separating film is, the higher the probability is for conduction. This explains why the total device conductance increases with pressure. Figure 1(a) shows the scheme of conduction, where y is the physical axis resembling the charge carriers (e^-) would move in a vertical path from the upper electrode towards the lower through the CPC. The height of the potential barrier depicted in Figure 1(a) is a consequence of the insulating characteristics

of the polymer matrix, which would avoid electrical conduction if the separating film were not that thin. Since this film is not thicker as some nanometers, quantum tunneling (QT) happens and charge carriers (e^-) may overcome the barrier. Let s_0 be the interparticle separation thickness when the FSR is not subjected to mechanical stress, and s_f be the thickness of interparticle separation when the device is subjected to stress, which accomplishes $s_f < s_0$. Figure 1(b) shows a simplified scheme of a FSR, where the black dots



(a)



(b)

FIGURE 5: Continued.

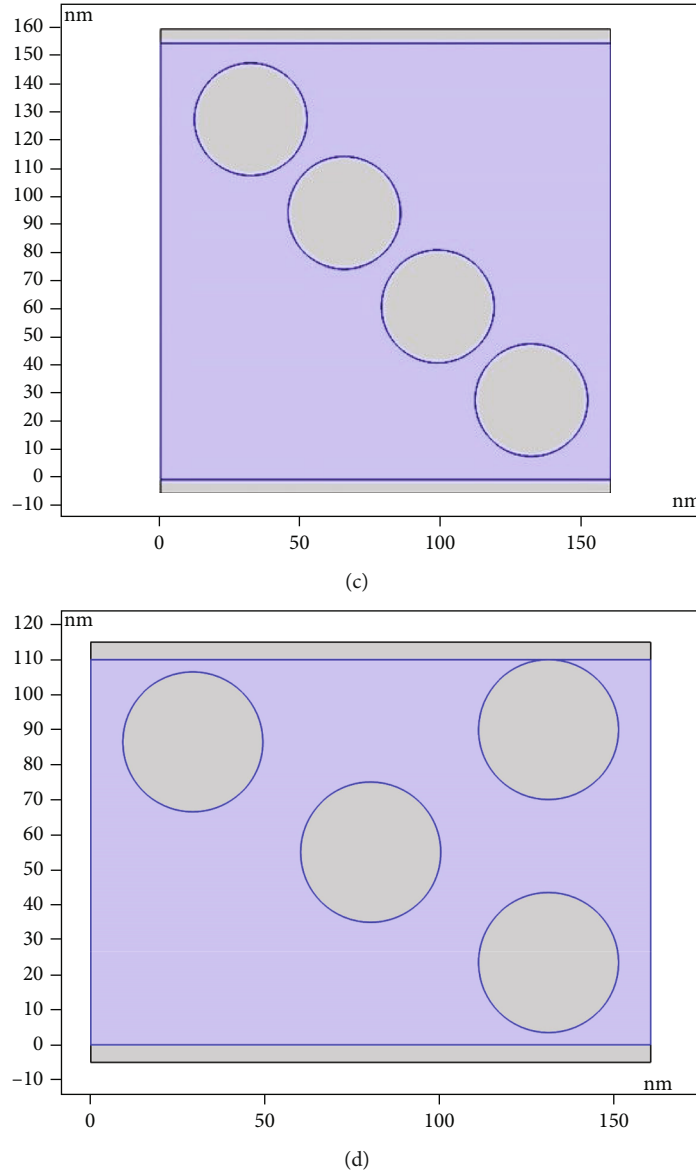


FIGURE 5: Geometries for each considered version of the model to simulate. From now on, the different versions of the model will be presented in all figures in the same order as they are in this one.

represent the conductive nanoparticles. Pressure σ_f causes the devices to shrink in the direction of force, as well as interparticle separation between neighboring nanoparticles. Since deformation depends on the exerted stress, it is depicted in Figure 1(a) as a function $s(\sigma)$, where σ is the exerted stress. Equations (1) through (3) are Simmons' approach that plenty of CPC models rely upon [4]. Based on Simmons' model for current density J through thin insulating films, relevant contributions have been proposed as follows:

$$J(u, s(\sigma)) = u \frac{3\sqrt{2m\varphi_0}}{2s(\sigma)} \left(\frac{e}{h}\right)^2 \exp\left(-\frac{4\pi s(\sigma)}{h} \sqrt{2m\varphi_0}\right), u \approx 0, \quad (1)$$

$$J(u, s(\sigma)) = \left(\frac{e}{2\pi h s(\sigma)^2}\right) \left\{ \left(\varphi_0 - \frac{eu}{2}\right) \exp\left[-\frac{4\pi s(\sigma)}{h} \sqrt{2m\left(\varphi_0 - \frac{eu}{2}\right)}\right] - \left(\varphi_0 + \frac{eu}{2}\right) \exp\left[-\frac{4\pi s(\sigma)}{h} \sqrt{2m\left(\varphi_0 + \frac{eu}{2}\right)}\right] \right\}, u < \frac{\varphi_0}{e}, \quad (2)$$

$$J(u, s(\sigma)) = \frac{2.2e^3 u^2}{8\pi h \varphi_0 s(\sigma)^2} \left\{ \exp\left[-\frac{8\pi s(\sigma)}{2.96 h e u} \sqrt{2m\varphi_0^3}\right] - \left(1 + \frac{2eu}{\varphi_0}\right) \exp\left[-\frac{8\pi s(\sigma)}{2.96 h e u} \sqrt{2m\varphi_0^3 \left(1 + \frac{2eu}{\varphi_0}\right)}\right] \right\}, u > \frac{\varphi_0}{e}. \quad (3)$$

The authors' previous work [6, 7] has proposed a conduction model for CPC-based FSRs, which predicts the value

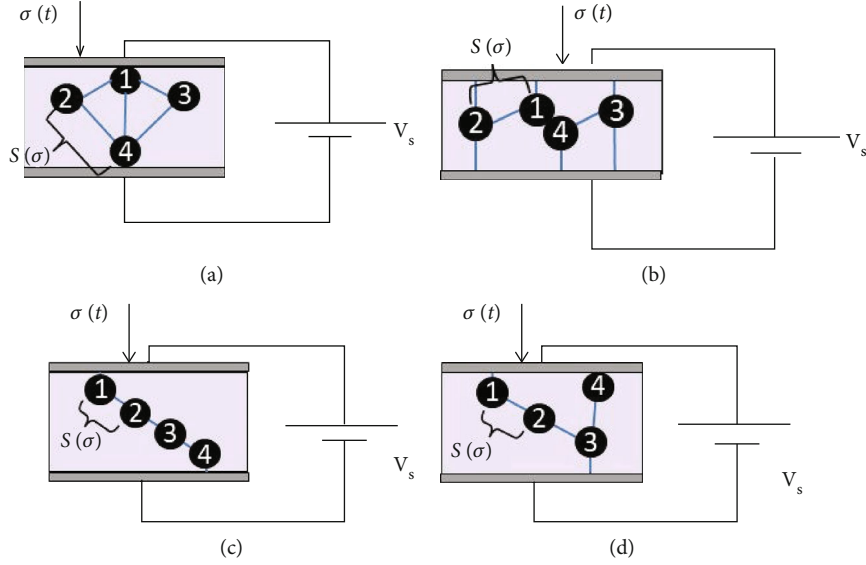


FIGURE 6: Some considered versions of the simplified “four-particle model.” $\sigma(t)$ represents the dynamic cycling loading stress to exert on the FSR. As a function of it, $s(\sigma)$ represents the interparticle separation. Blue lines represent a highly probable tunneling conduction path. V_s is the sourcing voltage.

TABLE 1: Model invariant parameters configured in the COMSOL Multiphysics framework which have been taken from results acquired in [6, 7]. Some of them are default parameters in materials library within COMSOL Multiphysics®.

Parameter	Version in Figure 5(a)	Version in Figure 5(b)	Version in Figure 5(c)	Version in Figure 5(d)
Matrix width	160 nm	165 nm	160 nm	160 nm
Matrix height	95 nm	85 nm	155 nm	110 nm
Electrode width			5 nm	
Electrode length	160 nm	165 nm	160 nm	160 nm
Particle radius			20 nm	
Burgers model parameters		$\eta_1 = 236.5 \text{ MPa}\cdot\text{s}, \eta_2 = 340.56 \text{ MPa}\cdot\text{s}, k_2 = 56.76 \text{ MPa}$		
PDMS Young’s modulus			750 kPa	
PDMS Poisson’s ratio			0.32	
PDMS electrical conductivity			0.1 S/m	
Silver Young’s modulus			83 GPa	
Silver Poisson’s ratio			0.37	
Silver electrical conductivity			$61.6 \cdot 10^{10} \text{ S/m}$	

of device’s resistance (or the current flowing throughout the device) for specific values of voltage and interparticle film thickness, and thus, applied pressure. Also, it includes the contact resistance, which is the opposition to the pass of charge carriers to the nanoparticle(s) physically contacting upper or lower electrodes or also contacting among each other.

- (i) Contact resistance: according to the proposed electrical model in Figure 2, voltage in R_{CPC} as a function of the sourcing voltage can be written as $u = V_s - R_C I$, where I is the circuit current (J by the effective conductive area). Contact resistance has been modeled by Kalantari et al. [5] and authors’ contributions have also led to an expression for contact resistance as a function of stress in (4). For the sake of simplicity,

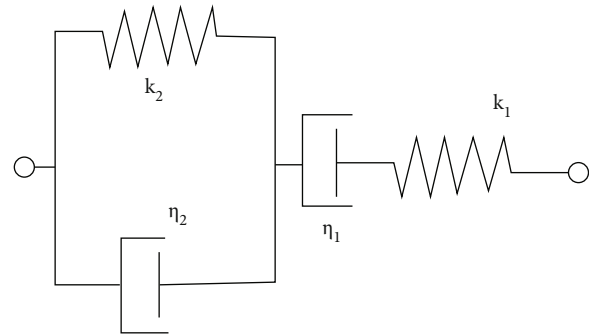


FIGURE 7: Burgers model were considered for simulations. See Table 1 for parameter reference set for dashpots (η_1 and η_2) and springs (k_1 , which is the Young modulus M , and k_2).

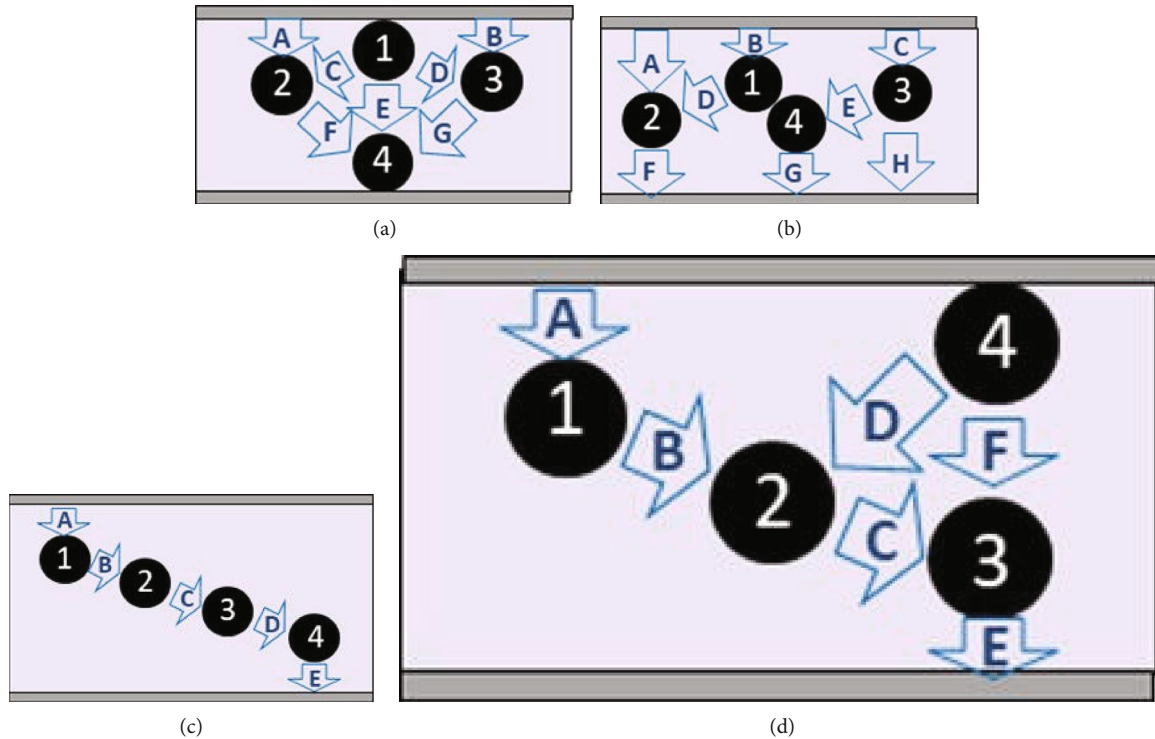


FIGURE 8: Label for each considered tunneling gap. Figures not to scale. Summary of labeling is in Table 2.

this equation has not been plugged in Equations (1) through (3). However, the authors' previous work [6] has managed to solve the equations as a function of V_S and I

$$R_c = R_{\text{par}} + \frac{R_c^0}{\sigma^k}, \quad (4)$$

where R_{par} is the particle resistance, R_c^0 the contact resistance at rest state (unloaded), and k is a form factor

- (ii) R_{CPC} depends on σ and V_S as the most independent variables according to Equations (1) through (3). At this stage, this approach has been used to analyze FSR performance for a relative wide range of sourcing voltages. The interparticle separation s as a function of σ is shown in

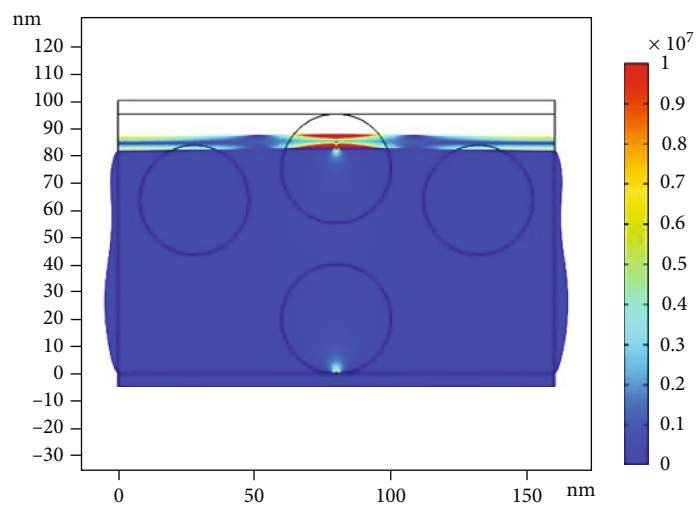
$$s(\sigma) = s_0 \left(1 - \frac{\sigma}{M}\right), \quad (5)$$

where s_0 is the interparticle separation at rest state and M is the polymer's Young modulus. The behavior of σ as a function of time when dynamic forces are exerted on the FSR has been thoroughly studied by authors' in [7], where rheological responses have been considered through the Burgers model.

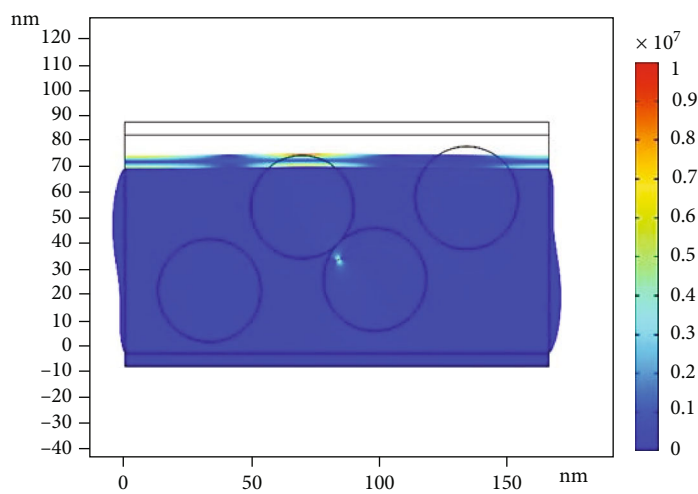
Figure 3 shows a plot of the full FSR resistance, which is the sum of R_{CPC} and R_c , for several values of sourcing volt-

age (0 V-7 V), and for a fixed stress of 250 kPa: ($R_{\text{CPC}} = u/AJ(u, s(250 \text{ kPa}))$), where A is the effective conductive area of the sensor. Contact resistance, as shown in Equation (4), does not depend on the sourcing voltage, so it remains unchanged for all voltages. Thus, FSR full resistance depends solely on the quantum tunneling (QT) phenomenon present in R_{CPC} . Moreover, Figure 3 also shows the sharp decrement of R_{CPC} and thus the full resistance for high values of sourcing voltage. This is a consequence of the QT phenomenon, where the higher the sourcing voltage is, the higher the probability of conduction across thin insulating films is due to the higher quantity of charge carriers provoked by higher sourcing voltages. Thus, R_{CPC} decreases dramatically when sourcing voltage is high because of this high probability of tunneling conduction.

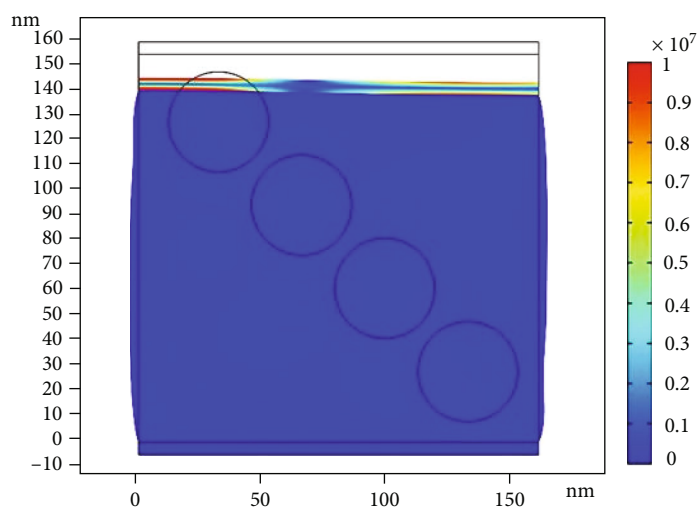
For very low ($u \cong 0$) Figure 3 shows what can be seen in Equation (1). Both sides of equation can be divided by u and multiplied by A , so an expression for conductance ($1/R_{\text{CPC}} = AJ(u, s(250 \text{ kPa}))/u$) can be obtained. Conductance/resistance happens to be nondependent on voltage, so this first part of the graph is constant, and the sensor behaves ohmic. Once the voltage rises, resistance becomes to be more dependent on voltage (see Equations (2) and (3), where no matter what operation is done, dependence on voltage cannot be eliminated) so the sensor is no longer ohmic and also very sharp in the drop of resistance over voltage. Due to the existing exponential functions in Equations (2) and (3), it is worth to remark how little the contribution of the contact resistance is for low voltages, where it only sums less than $10^4 \Omega$ for a total resistance of approximately $10^{12} \Omega$. This is caused by the high-resistance polymer



(a)



(b)



(c)

FIGURE 9: Continued.

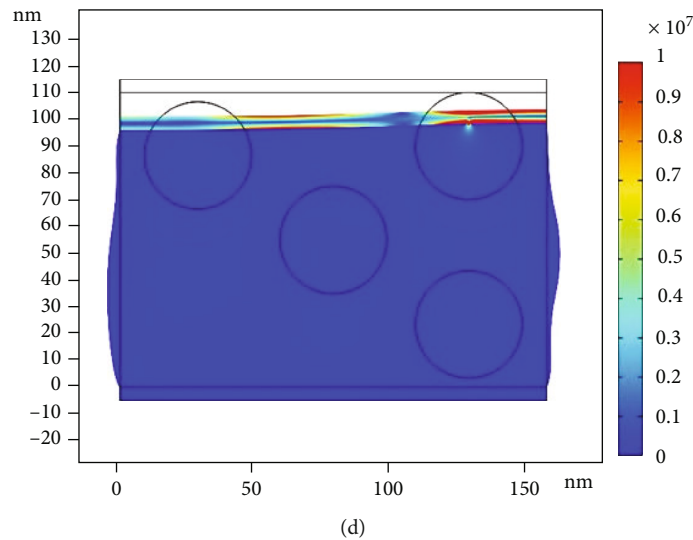


FIGURE 9: Von Mises stress at every point of the model for all its versions considered at the beginning of the time-dependent study ($t = 0$ s).

thin films offer when tunneling conduction probability is low due to low sourcing voltages. Conversely, contact resistance provides up to the half of the full resistance when sourcing voltage (and thus tunneling conduction probability) is high. This is an observation worth to bear in mind for the following explanations towards equipotential surface analysis.

3. Sensitivity Degradation

Sensitivity degradation (SD) is mainly observed in periodic loading application such as gait analysis. Measurements could be seriously misled if sensors loose sensitivity during the try. Figure 4(a) shows a constant pace gait pattern acquired with insoles where Flexiforce A201-1 sensors were deployed. However, it wrongly suggests that the pressure of lasts steps has experienced a lowering trend. Sensitivity degradation consists in a progressive reduction of the voltage/force sensitivity ratio due to periodic loading. This phenomenon complicates calibration. Characterization of the reducing trends of sensitivity ratio would be needed to compensate degradation for calibration or postprocessing in offline applications. However, authors have observed and reported sensitivity degradation as a voltage-dependent phenomenon [27]. For low sourcing voltages, sensitivity degradation has not been observed for long tries of cycling loading, whereas the degraded pattern such as that in Figure 4(b) are typical for a sourcing voltage higher than 7 V (9 V for the precise case of Figure 4(b)). Thus, the practical recommendation has been to select low sourcing voltages V_s to feed FSRs specially for periodic loading applications. Attention on sourcing voltage has been already called to enhance quality of force readings with FSRs. For instance, nonconstant voltages dropping in FSRs hinder repeatability. This fact relies on the dependence of FSR's resistance on voltage as shown in Equations (1) through (3). Hence, voltage dividers as driving circuits have been discouraged by authors when high repeatability of readings is

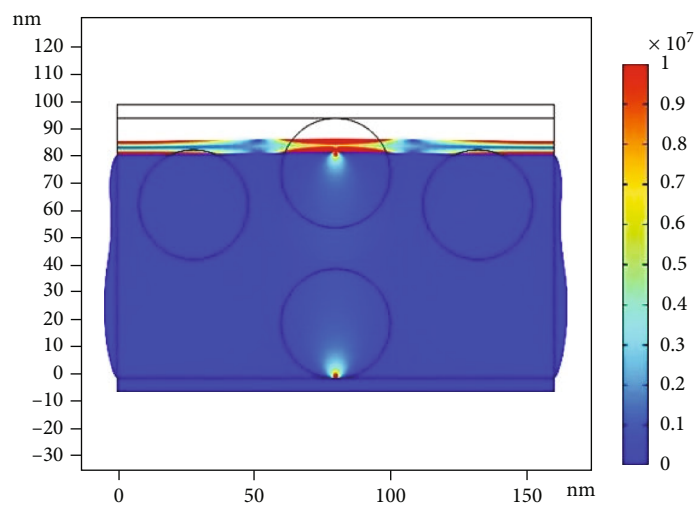
needed [27]. Driving circuits used for experiments in [28] guarantee constant voltage feeding for all FSRs in the insoles. However, a different signal was acquired when sourcing voltage was lower (1.27 V), *ceteris paribus*, see Figure 4.

Sensitivity degradation has also been reported in plenty of works [26, 29, 30] as a worrying and not fully understood phenomenon.

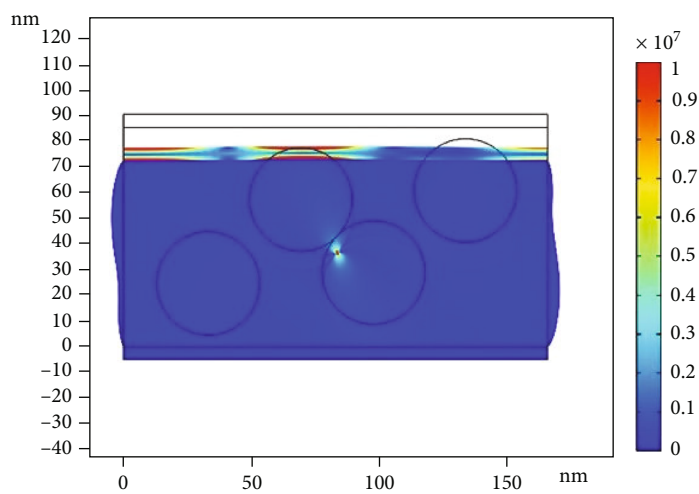
It is worth to remark that neither the deployed sensors nor the insoles presented any damage during the experiments. In fact, the non-descending trend observed when low sourcing voltage was applied is evidence of no degradation. Experimentally, dependence of sensitivity degradation on voltage has been clear as the only variable which causes degradation by periodical loading. Nevertheless, a theoretical explanation for this relation is still missing. The authors have hypothesized on the causes for sensitivity to degrade, and hence, a simplified model has been proposed to support it. Validation of hypothesis will be performed next through a finite element method approach since it relies upon the rheological behavior of the polymer matrix in an important extent.

4. Simplified “Four-Particle Model” for Finite Element Analysis

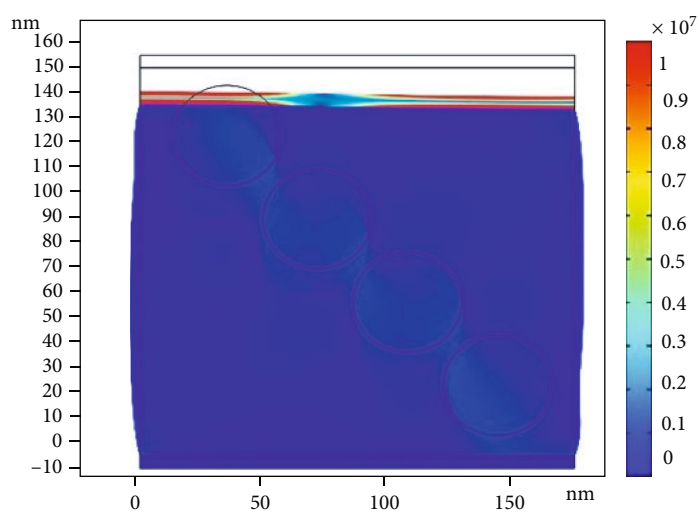
This section explains the so called “four-particle-model,” which is a simple representation of a FSR based in CPC with only four nanoparticles. This approach is considered enough for simulating phenomena of interest through finite element analysis (FEA), associated to contact, potential, and dynamics [31]. Moreover, the use FEA tools for MEMS devices such as FSR has been a helpful for plenty of research tasks [32–34]. Figure 5 shows four versions of this model, which is very similar to the one shown in Figure 1. Thus, polymer matrix and electrodes terminal are represented the same way. This section is intended to explain and justify each detail that composes this simplified model.



(a)



(b)



(c)

FIGURE 10: Continued.

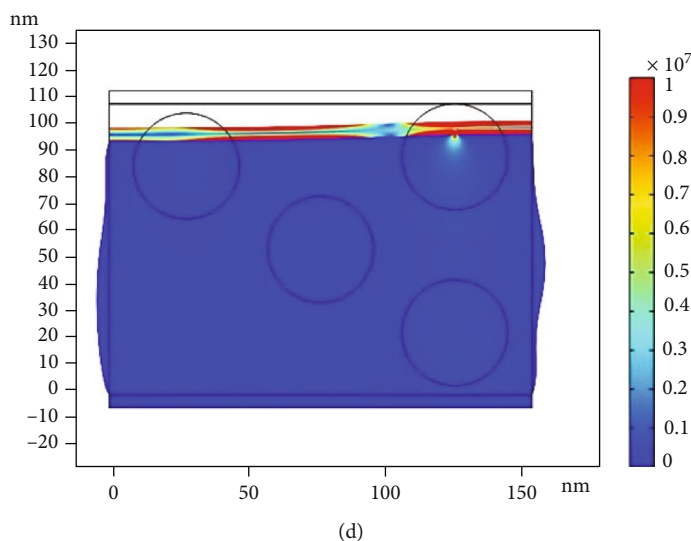


FIGURE 10: Von Mises stress at every point of the model for all versions considered at $t = 0.3$ s, when applied boundary loading approaches to the maximum.

TABLE 2: Tunneling gaps for each version of the “four-particle-model”. See Figure 8 for a graphic representation.

Gap	Between which elements model in Figure 8(a)	Between which elements model in Figure 8(b)	Between which elements model in Figure 8(c)	Between which elements model in Figure 8(d)
A	Upper electrode–particle 2	Upper electrode–particle 2	Upper electrode–particle 1	Upper electrode–particle 1
B	Upper electrode–particle 3	Upper electrode–particle 1	Particle 1–particle 2	Particle 1–particle 2
C	Particle 1–particle 2	Upper electrode–particle 3	Particle 2–particle 3	Particle 2–particle 3
D	Particle 1–particle 3	Particle 1–particle 2	Particle 3–particle 4	Particle 4–particle 2
E	Particle 1–particle 4	Particle 3–particle 4	Particle 4–lower electrode	Particle 3–lower electrode
F	Particle 2–particle 4	Particle 2–lower electrode	—	Particle 4–particle 3
G	Particle 3–particle 4	Particle 4–lower electrode	—	—
H	—	Particle 3–lower electrode	—	—

Figure 6 shows four versions of the model, where the fundamental difference among them is the different positioning of the particles in the matrix. Each version will show a different scenario of interparticle separation dynamics and how it affects the electrical response of the device. Some of them embrace the scenario of considerable contact resistance with the electrodes (6(a) and 6(d)) or among them (6(b)), which is an ohmic phenomenon that contributes to the full FSR resistance according to the electric model in Figure 2. As already shown, contact resistance needs to be considered apart since it does not rely upon QT and only depends on the mechanical stress and is voltage independent [5]. Further particles represent those QT occurs throughout. They are isolated from one another solely by polymer thin films that shrink due to the mechanical stress the device could be subjected to. It is considered in a sandwich-like fashion as the Flexiforce A201-X, which has been one of the most characterized devices in authors’ recent research [6, 7, 27, 35].

These “four-particle models” are the simplest approach to consider so the electrical response by periodic loading could be analyzed. It could be considered that these four particles are the smallest spatial sample to consider in the FSR device where the coupled mechanical and electrical phenomena that could provoke SD can be simulated.

All versions of the “four-particle model” will be subjected to electrical and mechanical boundary constraints in a FEA framework performed in COMSOL Multiphysics® Modeling Software to analyze their response under periodic loading conditions. The analysis involves an understanding of the electrical equipotential surfaces that arise due to the sourcing voltage and the dielectric conditions existent in CPCs. However, it is worth to pay attention on the fact that the dielectric role played by the polymer insulating matrix could be also conditioned by the mechanical conditions of periodic loading, contact resistance, and the rheological conditions of polymers [36, 37]. This framework allows to analyze both coupled effects and thus, the shown versions of the “four-particle model” have been implemented in the

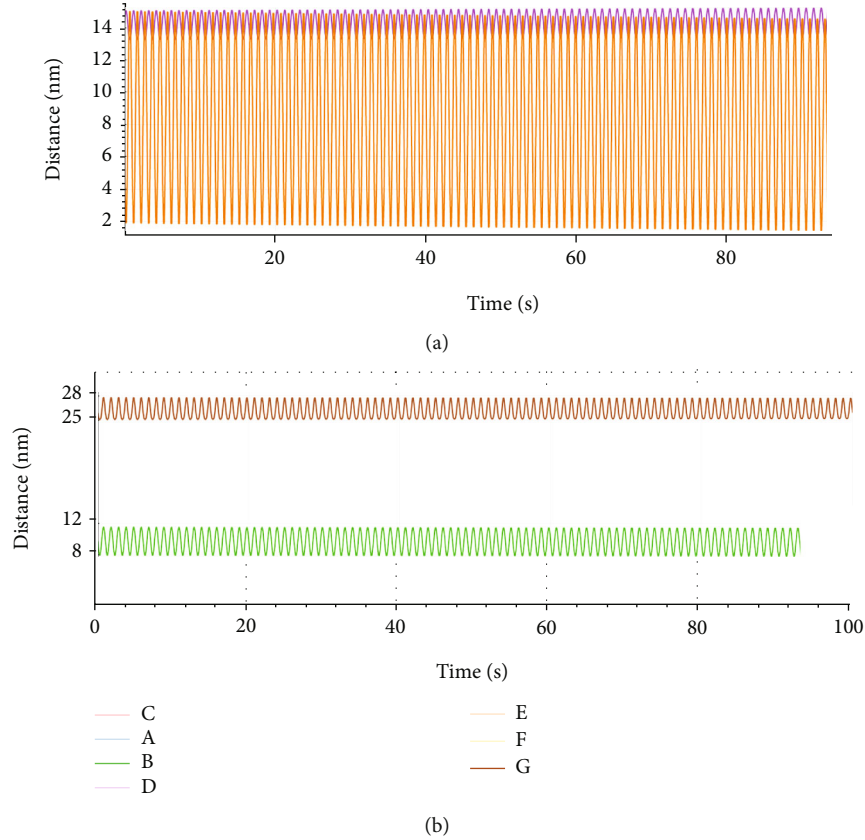


FIGURE 11: Some of the distances of the tunneling gaps in version of the four-particle-model in Figure 8(a).

framework this software provides. FEA has been widely used for microelectromechanical systems (MEMS) due to the possibility of analyzing both coupled electrical and mechanical physics and particularly for sensing devices [38]. The technical details of the model and the executions of simulations to validate the aforesaid ideas are exposed next.

For FEA model geometry, Figure 5 shows the model geometry of the four-particle model built in COMSOL Multiphysics® with the physical parameters from studies in [6, 7]. Some other values have been measured directly from Flexiforce A201-X commercial sensors or taken from data-sheets. Also, default parameters of materials library COMSOL Multiphysics® offer have been considered.

For FEA model materials, Figure 5 shows the domains that represent the polymer matrix, whose material has been configured to PDMS (polydimethylsiloxane), present in the COMSOL Multiphysics framework. Silver has been assigned to be the material the nanoparticles, and terminals are made of since it is an isotropic material widespread used for commercial force sensing devices [39, 40]. This setting provides electrical conductivity and mechanical parameters to the simulations to perform. Parameters to set have been presented in Table 1.

Two interfaces were added to the model to simulate the most important physical phenomena occurring when sensor is subjected to mechanical stress and sourcing voltage. *Electrical currents* and *solid mechanics* interfaces' conditions are described next.

Electric current interface–current conservation consists in a low-voltage stationary study where equations to solve are

$$\begin{aligned} \nabla \cdot J &= Q, \\ J &= \sigma \vec{E} + J_{\text{ext}}, \\ \vec{E} &= -\nabla V, \end{aligned} \quad (6)$$

where J is the current density; Q is the electric charge; J_{ext} is any electrical external current density; σ is the electrical conductivity, whose value comes from the previously configured material; \vec{E} is the electrical field; and V the electrical potential. Room temperature of 293.15 K has been set for all simulations.

For electric current interface–terminals, the potential V comes from the configuration made for both terminals. The lower is set to ground whereas the upper is set to the voltage V_s , whose setting depends on the simulations to run. In order establish a comparison with the results in [28], two simulations must be considered: One at low voltage (1.27 V) and other at higher voltage (9 V).

For electric current interface–contact impedance, when any particle physically contacts the upper terminal or touches another particle, there is contact resistance R_C that must be considered. This is set differently depending on the study to perform and has been set according to the explanations of Section 2.

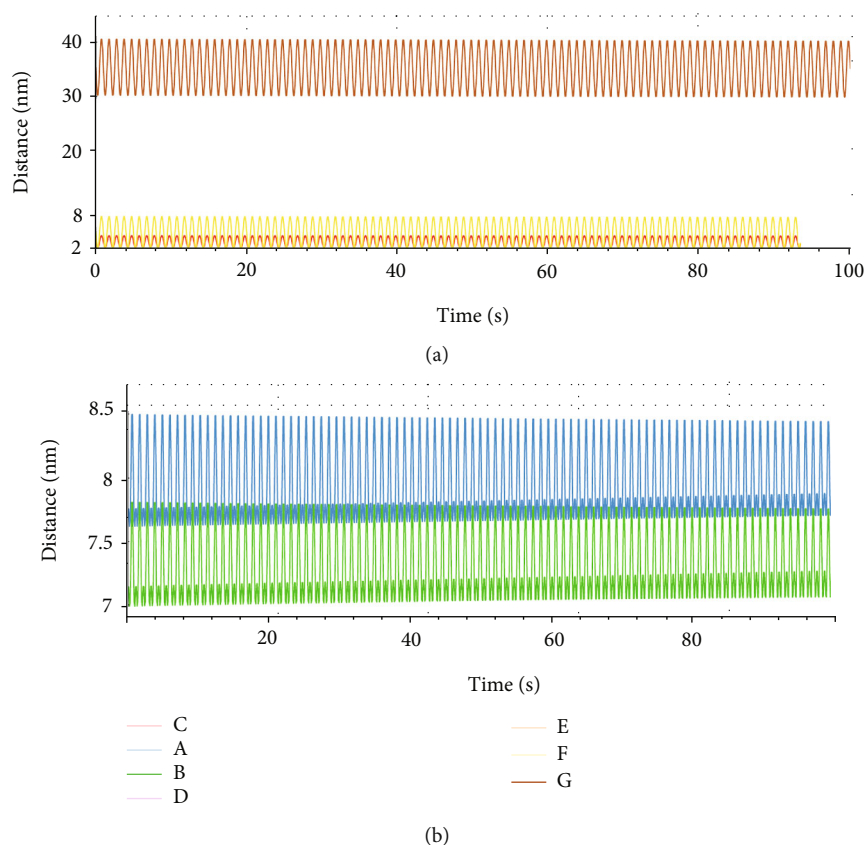


FIGURE 12: Time plots for interparticle tunneling gaps *A*, *B*, and *C* (a) and *D* and *E* (b) in version of the model in Figure 9(b).

- (iii) If the voltage to set is 1.27 V, since the R_{CPC} resistance is up to eight orders of magnitude higher, what makes contact resistance negligible. It has been set to zero in the corresponding COMSOL Multiphysics® node
- (iv) If the voltage to set is 9 V, the contact resistance cannot be neglected, so it has been set to a non-zero value in the corresponding node. Section VI in this paper provides a more detailed explanation in this regard

For electric current interface–other boundary conditions, external boundaries of all models have been set to be electrically isolated, except the lower one, which was set to ground as previously explained. All initial values have been set to zero, which means that every component of the model starts at the same electric potential and there is not electrical charge in any part of the model.

For solid mechanics–linear elastic material, a Burgers model (Figure 7) has been set for the mechanical dynamic study at room temperature. It is worth to recall that these settings are made for the PDMS matrix, which is the violet domain shown for each version of the model in Figure 5. Burgers model parameter is taken from [6]. Since electrodes and particles are set to be made of a highly stiff material such as silver, viscoelastic features are secondary to the extent that some of them were not needed to be set.

For solid mechanics–boundary load, to simulate some gait-like loading patterns, Equation (7) was set as the dynamic periodic pressure to exert on the upper electrode. Hence, pressures from 0 to 300 kPa have been simulated with a frequency of one cycle per second.

$$\sigma(t) = 150 + 150 \sin(2\pi t). \quad (7)$$

For solid mechanics–other boundary conditions, lower electrodes are not allowed to move in any direction whereas the upper only is allowed to move along the vertical axis. All components in the model start from rest.

For electrical probes, there are measuring probes to acquire the voltage between neighboring nanoparticles and, when needed, between nanoparticles and electrodes. These readings are needed to be the voltage u in Equations (1) through (3). For every version of the model, there are interparticle or electrode-particle gaps (from now on called tunneling gaps) to take into consideration. Since potential condition does not change over time, they have been acquired with two “Stationary Studies” nodes in COMSOL Multiphysics®, one for each sourcing voltage (1.27 V and 9 V). Figure 8 shows how they have been labeled in this work.

For mechanical probes, as well as voltage needs to be measured with probes for each tunneling gap, their distance at any moment of the simulation is also needed since it is the parameter s in Equations (1) through (3). They have been

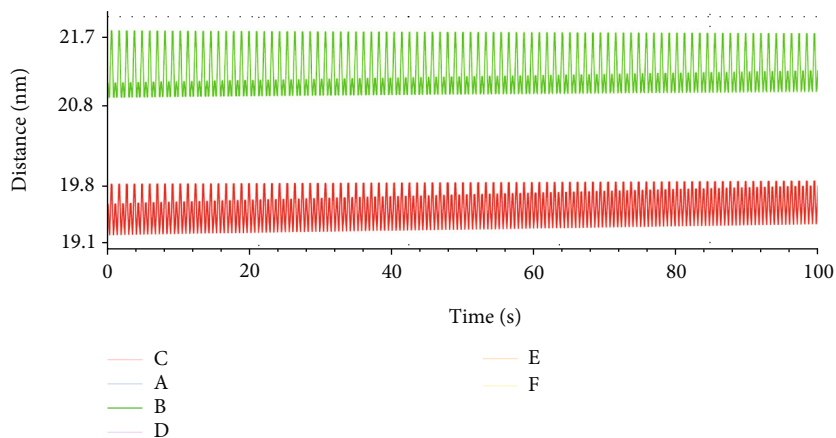


FIGURE 14: Nonvertical gaps C and D in version of the four-particle model in Figure 5(d). D gap decreases whereas C gap increases.

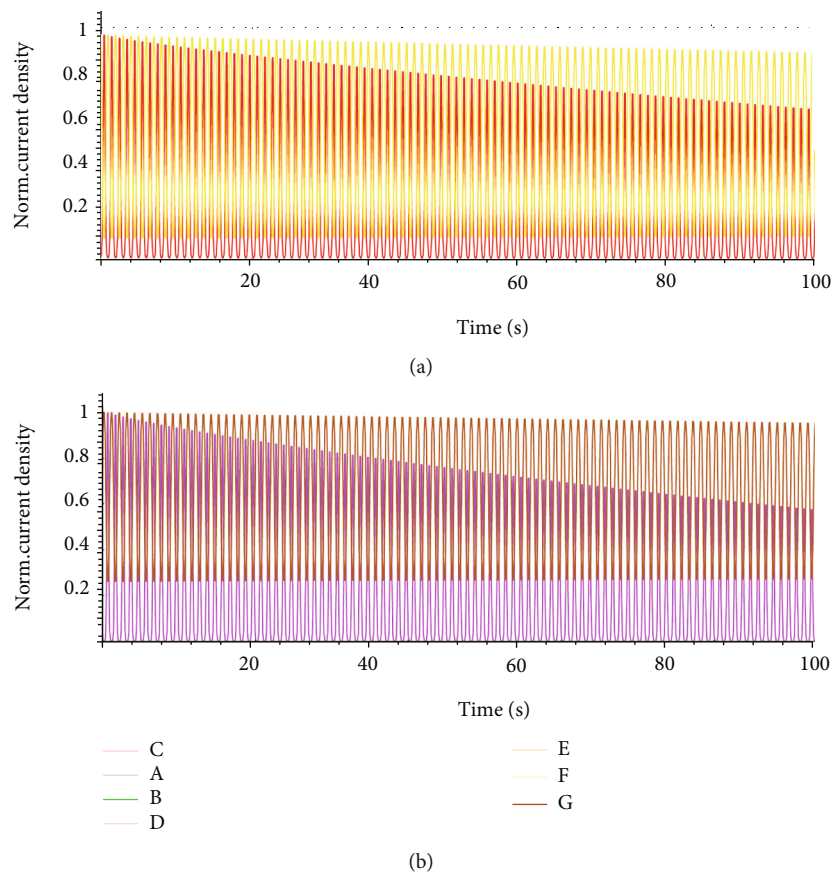


FIGURE 15: Normalized currents for gaps C nad F (a) and D and G (b) for version of the four-particle model in Figure 5(a).

affect interparticle distances for some loading patterns. If loading period is short enough, the recovering phase at unloading half-cycle may have not ended when the next loading half-cycle begins. This provokes a striking trend in inter-particle separation by periodic loading which affects also the tunneling conduction between neighboring particles.

Additionally, rheological behavior also involves related responses to its low Poisson ratio. Polymer matrix material

exhibits considerable expansion in its radial direction when the exerted force goes in the normal direction. Thus, this slow recovery phase by unloading half-cycle is not observed as an expansion in the normal direction but also as a contraction in the radial one. The interparticle separations experience different trends because of this dynamic behavior depending on the interparticle tunneling gap under scope. Hence, a time-dependent study has been carried out, as described before in COMSOL Multiphysics®, to understand

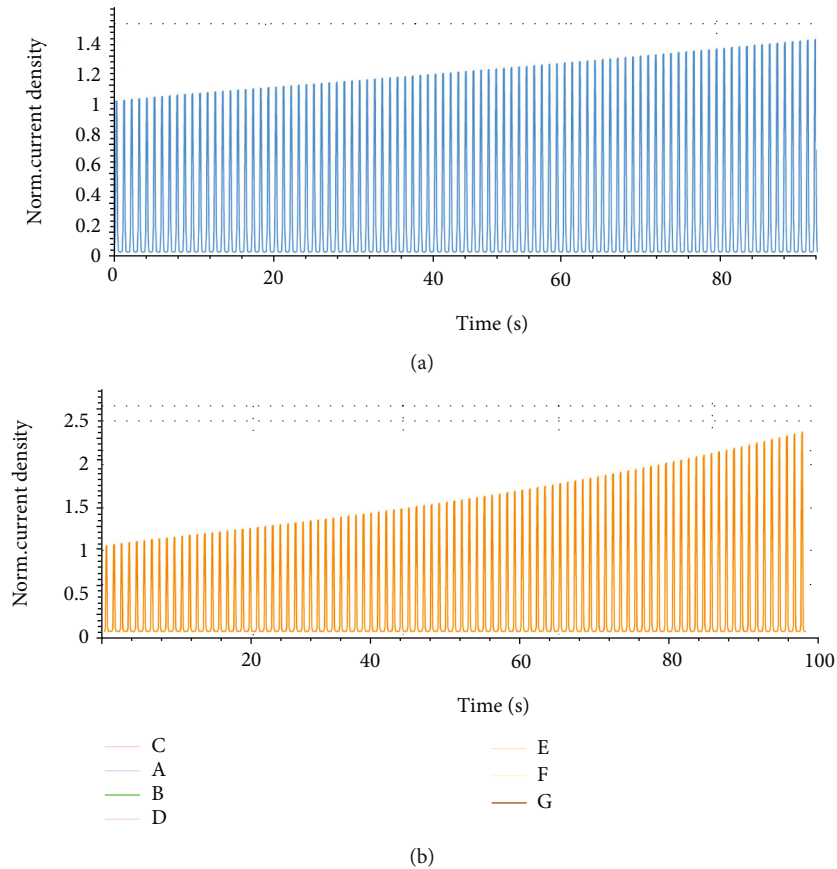


FIGURE 16: Normalized current through gaps *A* and *E* in version of the model inf Figure 5(a).

how interparticle distances evolve under periodic loading. Equation (7) shows how much pressure has been considered and how frequent the loading pattern is. Figures 9 and 10 show the von Mises stress for every point of all versions built of the four-particle model.

Although some measurements of the von Mises stress are shown in this work, the most important result of the mechanical simulation has been the distance between neighboring particles with special scope in the labeled tunneling gaps depicted in Figure 8 and organized in Table 2. For version in Figure 8(a), some distances of tunneling gaps are shown in the following time plots in Figure 11. Gaps *E* (with its particles positioned on a vertical line) and *D* (with its particles positioned on a nonvertical line) in Figure 11(a) have been selected to be shown since they represent two of the different trends observed in the simulation. Gap *E* maximum of each cycle is slightly lower than the former one, whereas Gap *D* shows a totally different trend: Its maxima are each time slightly higher. In Figure 11(b), similar trends have been also observed. Gap *G* has an increasing trend whereas Gap *B* decreases. For all time plots, increments or decrements are perceptible after long enough simulations.

Gap *A* distance is highly correlated with gap *B* as well as Gap *F* with Gap *G*, and Gap *C* with *D*. This relies upon the fact of the high symmetry this version of the model exhibits. Gaps *A*, *C*, and *F* correspond symmetrically with *B*, *D*, and

G, respectively. Hence, only time plots for *B*, *D*, *E*, and *G* are shown in Figure 12.

For the rest of the versions these both trends have been also observed with a relevant detail. Increasing trends are observed for interparticle tunneling gaps whose particles are placed in a mostly vertical fashion, whereas decreasing trends show up when the conducting path between particles has any considerable horizontal component (or radial component, due to the disc shape of the sensor, which would be radial in cylindrical coordinates). The more horizontal (radial) component the path has, the more the trend of the distance decreases with every cycle. This observation matched with the expectations due to the rheologic characteristics of the polymer matrix. The observed increasing trend relies upon low Poisson's ratio since the exerted force goes in the normal direction, so the polymer expands in the horizontal (radial) one.

These mostly vertical gaps, called from now on in this paper "vertical gaps" present this decreasing behavior due to the creep features the polymer matrix present. When the unloading half-cycle starts, it begins to recover to the rest positions and distances. Due to creep, recovery takes longer, and the device does not reach the rest position before the next loading half-cycle begins. Thus, two neighboring vertical particles facing a periodic loading force pattern would be closer with each cycle. Conversely, this uncomplete recovery

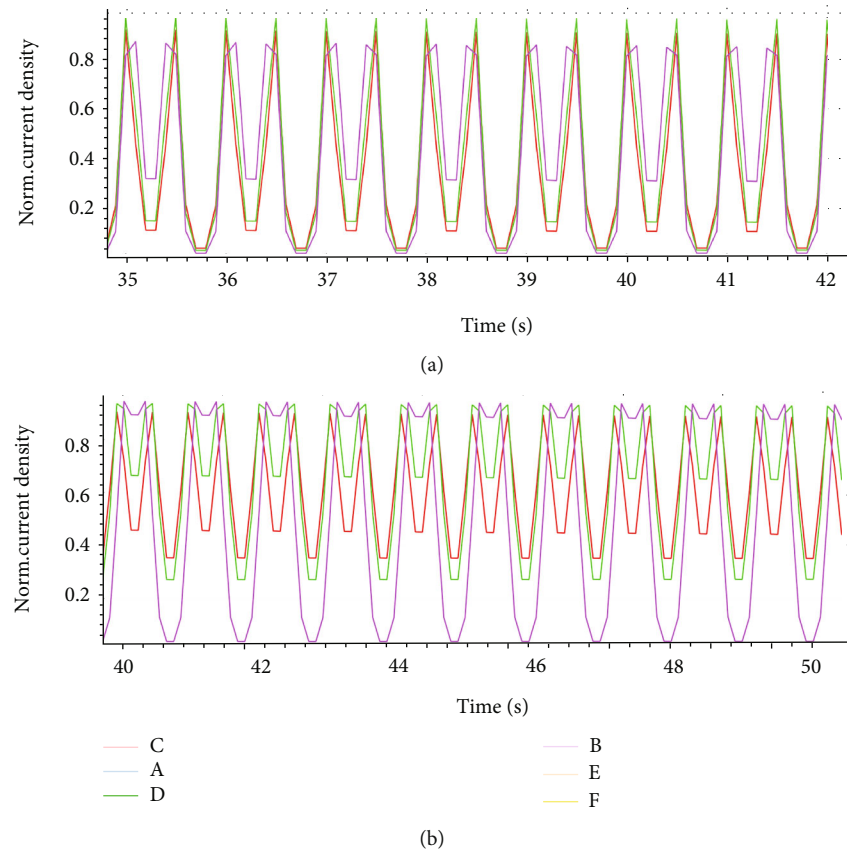


FIGURE 17: Closer version of some timeplots that show a secondary peak. (a) Version of the model in Figure 5(c) and (b) for version in Figure 5(d).

is also observed in the horizontal (radial) axis. However, these “nonvertical gaps” exhibit quite different trends among them for each cycle. The less vertical the gap is (see timeplot for gap *D* in Figure 11(a) and timeplot for gap *G* in Figure 11(b)), the more ascending the pattern is. Thus, two particles next to each other at similar heights, what could be called a “horizontal gap,” with each loading cycle would be each time further away from each other. Nevertheless, horizontal (radial) component of the gap must be considerable, so the resulting distance can exhibit an increasing trend, see Figures 13 and 14.

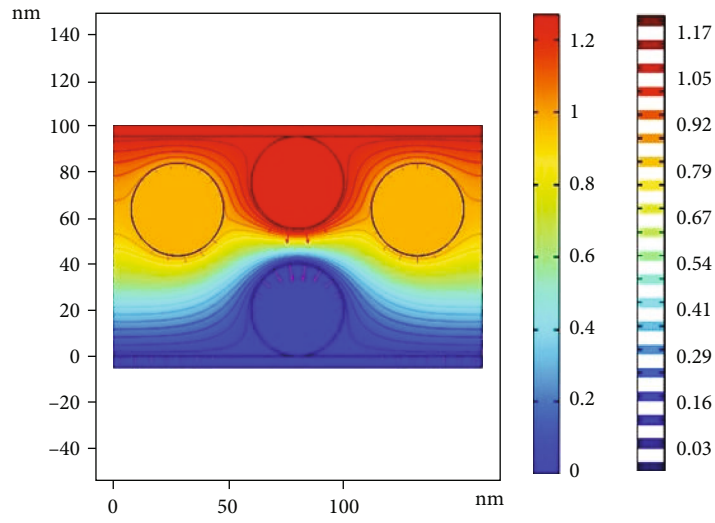
The most relevant fact related to these trends of distance between neighboring particles is its dependence on the tunneling resistance. The FEA simulation has also provided the voltage for each tunneling gap, and their analysis will be presented in the next section. However, once the interparticle separation and voltages for each gap are computed, the current density J can be calculated with Equations (1) through (3). Thus, the contribution of all gaps in scope can be known. Since mean distances for all gaps in all versions of the model are very different, normalized J will be presented next. Normalization has been performed with the maximum of the first loading cycle.

Figure 15 shows what was expected for gaps *C*, *D*, *F*, and *G* nonvertical gaps: The current density J shows a decreasing trend of its maxima due to the increasing trend of the inter-

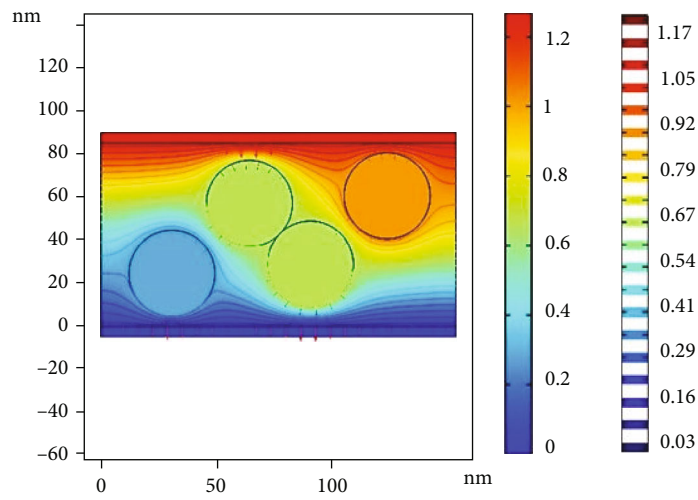
particle separation. Since the bigger the gap is, the lower the probability for tunneling conduction becomes and that is why a descending current density trends are observed for nonvertical conduction gaps. It is also worth to remark how noticeable the descending trend in J is although the trends in interparticle separation are slightly increasing. Figure 16 shows J for the vertical gaps *A* and *E* (*B* is not shown since it is similar to *A*, due to symmetry), which are increasing as expected.

Although FEA simulation has been executed for two different electrical nodes with different sourcing voltages ($V_s = 1.27\text{ V}$ and $V_s = 9\text{ V}$), current density time plots acquired from each condition are not distinguishable due to normalization. However, for the following analysis, voltage is not yet relevant.

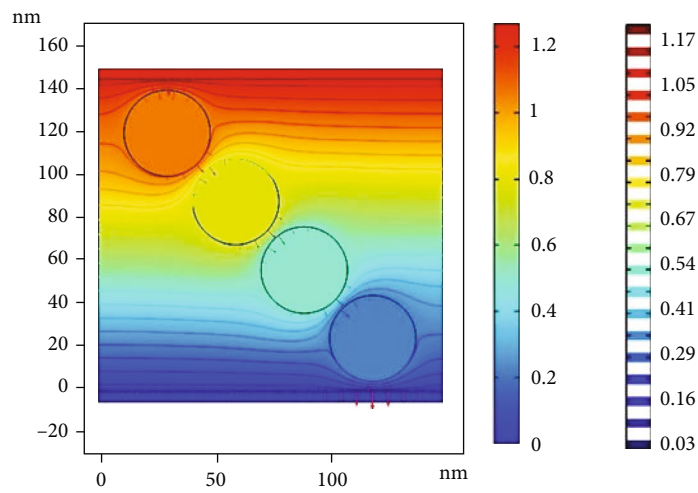
For nonvertical gaps, it is worth to pay high attention to the descending current density trend of maxima immediately recalls to sensitivity degradation. Figure 16 shows how this descending trend is more notorious for those paths with more horizontal (radial) component. However, increasing trend is dramatically increasing for vertical gaps. Thus, this analysis suggests that, if sensitivity degradation occurs because of tunneling conduction through nonvertical paths, there must be an additional condition that makes nonvertical conduction predominate. As formerly exposed, sensitivity degradation is observed for high sourcing voltages.



(a)



(b)



(c)

FIGURE 18: Continued.

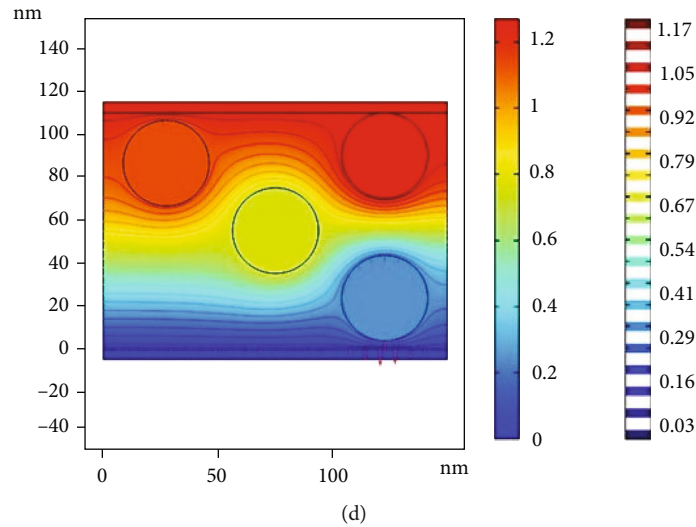


FIGURE 18: Potential distribution (rightmost scale in each figure) and equipotential surfaces (scale in the middle of each figure) for low 1.27 V sourcing voltage for all versions of the model. Red arrows represent the electric field.

Thus, considering sensitivity degradation as a voltage-related phenomenon, an electrical analysis must be carried out so its influence can be assessed.

Additionally, there is an extra detail to pay attention to. Figure 17 shows some sort of a secondary peak in the time plot, which has also been observed for interparticle separation in Figures 13–15. These “secondary peaks” have also been reported in [29, 30] as an extra concerning phenomenon associated to periodic loading.

6. Electrical Stationary Analysis

The FEA COMSOL Multiphysics® analysis carried out for this work involves two different voltage sourcing conditions: 1.27 V, which does not show any important degradation in sensitivity, and 9 V, in which sensitivity degrades to worrying extents. It is worth to recall that contact resistance to tunneling resistance proportion relies upon sourcing voltage as explained at the end of Section 2 (see Figure 3). The following FEA electrical analysis has paid the most attention to equipotential surfaces formed in the sensing device. The behavior of these surfaces will depend on the proportion of contact resistance R_C and the tunneling resistance R_{CPC} . As Figure 3 shows, when sourcing voltage is low, the total device resistance is composed predominantly by R_{CPC} , which is $>10^8 \Omega$ higher than R_C , making it negligible. Conversely, this dramatical difference between both resistances is not that large when sourcing voltage is high. Due to the higher probability of tunneling conduction at higher voltages, R_{CPC} decreases to the extent that it could be close to R_C values. Thus, the full device resistance will be comparable between R_{CPC} and R_C and no longer negligible. Two electrical conduction nodes in the COMSOL Multiphysics® Model Builder have been configured, where contact resistance is set to 0 for low sourcing voltage (1.27 V) and a higher value for high sourcing voltage (9 V). This higher resistance was calculated according with the discrete considerations presented

in [41–43] about the quantum point contacts. Equations (8) and (9) are needed to understand how contact resistance has been set in the model.

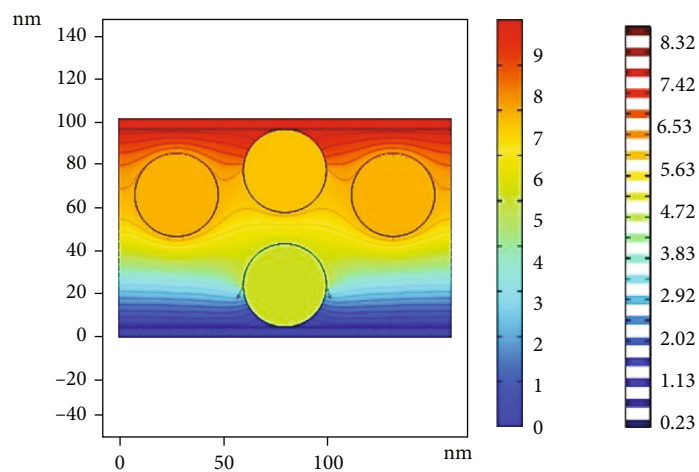
$$G_0 = \frac{2e^2}{h}, \quad (8)$$

$$L_{\text{par}} = n \frac{2\pi\hbar}{\sqrt{2mE_f}}, \quad (9)$$

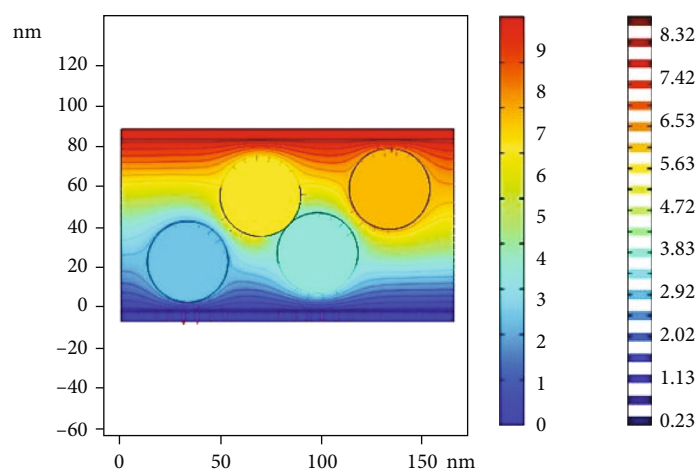
where G_0 is the discrete increment of contact conductance, L_{par} the length of the contact, and E_f the Fermi level. The smallest integer n that makes Equation (9) match will define how many G_0 increments will sum up the full contact conductance and its inverse has been set as contact resistance ($R_C = 1/n \cdot G_0$). For all simulations, R_C yielded 12906Ω , what is in the expected magnitude according to previous experiments where contact resistance has been calculated [5, 6].

Figure 18 shows the electric potential in the whole device when sourcing voltage is 1.27 V. In the models where any kind of contact between parts exists, same potential is observed for both contacting parts, since contact resistance is negligible. Thus, high potential differences are seen for, say, gap E in version of the model in Figure 18(a), what also favors a more intense electric field. Two contacting particles are present in version of the model in Figure 18(b). Hence, both are at the same potential and thus, a more intense electrical field is present in gap G (see Figure 8(b)).

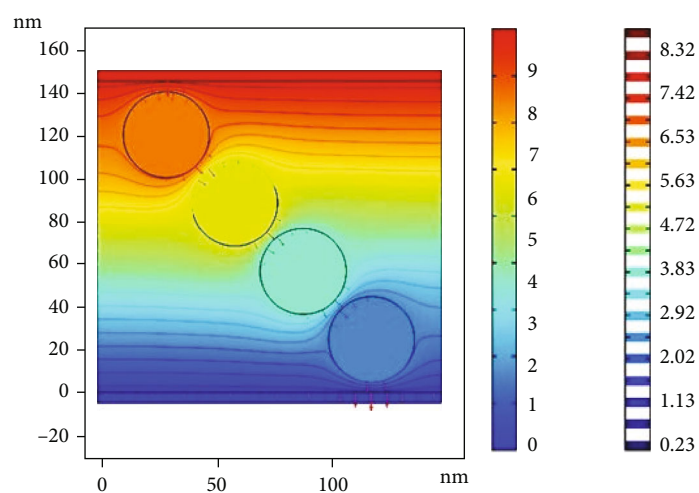
On the other hand, Figure 19 shows the same study with a sourcing voltage of 9 V, *ceteris paribus*. In the version of the model where there is any kind of contact, the voltage drop could be up to the half of the total voltage drop through the device since both R_C and R_{CPC} resistance could be similar. Thus, electrical potential changes significantly, except for version of the model in Figure 19(c), in which no contact



(a)



(b)



(c)

FIGURE 19: Continued.

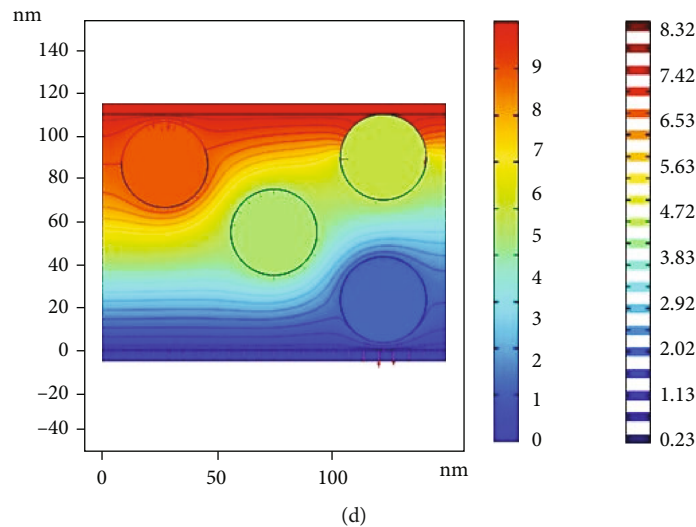


FIGURE 19: Potential distribution and equipotential surfaces for low 9 V sourcing voltage for all versions of the model. Red arrows represent the electric field.

situation has been considered. Comparing Figures 18(b) and 19(b), for instance, offers an idea of how potential changes affect the arousal of electrical fields in some other parts of the devices. Instead of a more intense electrical field in gap G in Figure 18(b), in Figure 19(b), this field is more notorious for gap E, which is nonvertical. In Figure 18(a), the high potential difference in gap E has decreased in comparison with Figure 19(a). Also, for Figures 18(d) and 19(d), there are quite notorious differences between the potential differences in gap F. Thus, the solely presence of a more considerable contact resistance, which arises due to higher sourcing voltages, provokes changes in the potential spatial distribution that in the simulated cases, favor conduction through nonvertical gaps rather than through vertical ones, because the higher the voltage in a certain gap is, the higher the probability of tunneling conduction becomes. Favoring conduction through nonvertical gaps means favoring it also through time-increasing tunneling resistances. This explains why high voltages, which are responsible of bending over equipotential surfaces and forcing electric field directions to be also nonvertical, causing the tunneling current to flow through particles which experience an increasing trend in their separation and therefore an increasing resistance, which leads to observe a time-decreasing current (sensitivity degradation), as seen in Figure 4 by the insoles experiment. As it is for the sensors in the insoles, this is an only voltage related phenomenon since it needs the electric field to be nonvertical. For low voltages, simulations show a mostly vertical direction for electric field, not favoring conduction through increasing gaps. This explains why SD is not observed for low voltages and only arises when sourcing voltages are high, as seen in Figure 4.

7. Conclusions and Ideas for Future Work

Calculating the whole device current with all tunneling contributions from each gap is not a straightforward task. Ran-

dom dispersion of nanoparticles in the polymer matrix hinders the process of finding out a general and accurate expression for current. Moreover, the high amounts of particles in a single specimen make any full model execution computationally too expensive. However, this 2D FEA model approach is a simple beginning to shed some light to more complete endeavors. Considering four particles have been the simplest representation found to portray the two desired key phenomena that provoke SD (increasing trend of interparticle separation maxima and equipotential surfaces modification due to contact resistance). It is logical to think that taking this model to the next level would be adding a third dimension. Any 3D model built under the consideration made in this work would increase the possibilities of the so-called nonvertical tunneling conduction gaps, since the third dimension to add would be orthogonal to the conducting downwards direction. Results in this work encourages to go forward in 3D modeling, but also it is worth to bear in mind that full accuracy could anyway be not reachable, and version of the models could be never-ending.

Nevertheless, this study also opens a window to lessen undesirable consequences of SD, which relies on voltage-related phenomena according with the potential consequences for high sourcing voltage. It has been already recommended to consider low sourcing voltage for applications where SD may mislead measurements. However, manufacturing considerations to reduce contact resistance could also avoid the bending over of equipotential surfaces and permit higher sourcing voltage, which are normally desired for boosting signal-to-noise ratios in acquired readings. This works also motivates to experiment in modifying manufacture protocols aiming to lessen contact resistance.

Data Availability

Data can be found in the Supplementary Information files: Palacio, Carlos (2021), "Finite Element Analysis Approach

for Sensitivity Degradation in Force Sensing Resistors,” Mendeley Data, V1, doi:10.17632/5z2gd75v7z.1

Conflicts of Interest

The authors declare that there is no conflict of interests.

Acknowledgments

The author Carlos Palacio acknowledges the Antonio Narriño University under project number 2021011-PI/UAN-2021-704GIFAM. The author Arnaldo Matute acknowledges the Juan De Castellanos University Foundation under project number CI00120-3.

References

- [1] F. Vecchi, C. Freschi, S. Micera, A. M. Sabatini, P. Dario, and R. Sacchetti, “Experimental evaluation of two commercial force sensors for applications in biomechanics and motor control,” in *Ann. Conference. of the International Functional Electrical Stimulation Society*, pp. 45–54, Aalborg, Denmark, June 2000.
- [2] D. Bloor, K. Donnelly, P. J. Hands, P. Laughlin, and D. Lussey, “A metal-polymer composite with unusual properties,” *Journal of Physics D: Applied Physics*, vol. 38, no. 16, pp. 2851–2860, 2005.
- [3] A. Lantada, P. Lafont, J. Muñoz, J. Munoz-Guijosa, and J. Echavarri, “Quantum tunnelling composites: characterisation and modelling to promote their applications as sensors,” *Sensors and Actuators A: Physical*, vol. 164, no. 1-2, pp. 46–57, 2010.
- [4] J. Simmons, “Electric tunnel effect between dissimilar electrodes separated by a thin insulating film,” *Journal of Applied Physics*, vol. 34, no. 9, pp. 2581–2590, 1963.
- [5] M. Kalantari, J. Dargahi, J. Kovacs, M. G. Mardasi, and S. Nouri, “A new approach for modeling piezoresistive force sensors based on semiconductive polymer composites,” *IEEE/ASME Transactions on Mechatronics*, vol. 17, no. 3, pp. 572–581, 2012.
- [6] L. Paredes-Madrid, C. A. Palacio, A. Matute, and C. A. Parra Vargas, “Underlying physics of conductive polymer composites and force sensing resistors under static loading conditions,” *Sensors*, vol. 17, no. 9, 2017<http://www.mdpi.com/1424-8220/17/9/2108>.
- [7] L. Paredes-Madrid, A. Matute, J. O. Bareño, C. A. Parra Vargas, and E. I. Gutierrez Velásquez, “Underlying physics of conductive polymer composites and force sensing resistors a study on creep response and dynamic loading,” *Materials*, vol. 10, no. 11, 2017<http://www.mdpi.com/1996-1944/10/11/1334>.
- [8] L. Wang, “Piezoresistive sensor based on conductive polymer composite with transverse electrodes,” *IEEE Transactions on Electron Devices*, vol. 62, no. 4, pp. 1299–1305, 2015.
- [9] S. Stassi, A. Sacco, and G. Canavese, “Impedance spectroscopy analysis of the tunnelling conduction mechanism in piezoresistive composites,” *Journal of Physics D: Applied Physics*, vol. 47, no. 34, article 345306, 2014.
- [10] L. Paredes-Madrid, L. Emmi, E. Garcia, and P. Gonzalez de Santos, “Detailed study of amplitude nonlinearity in piezoresistive force sensors,” *Sensors*, vol. 11, no. 9, pp. 8836–8854, 2011.
- [11] A. Damilano, A. Lince, S. Appendino et al., “Commercial tactile sensors for hand exoskeletons: practical considerations for ultra-low cost and very-low complexity read-out,” *IEEE Instrumentation Measurement Magazine*, vol. 19, no. 5, pp. 49–56, 2016.
- [12] L. Wang, “Variations in the capacitance and dielectric constant of multi-wall carbon nanotube filled silicone rubber composite during compressive creep,” *Composites Science and Technology*, vol. 130, pp. 1–8, 2016.
- [13] J. Dabling, A. Filatov, and J. Wheeler, “Static and cyclic performance evaluation of sensors for human interface pressure measurement,” in *Annual International Conference of the IEEE Engineering in Medicine and Biology Society*, pp. 162–165, San Diego, CA, USA, August 2012.
- [14] A. Matute, L. Paredes-Madrid, G. Moreno, F. Cárdenas, and C. A. Palacio, “A novel and inexpensive approach for force sensing based on fsr piezocapacitance aimed at hysteresis error reduction,” *Journal of Sensors*, vol. 2018, Article ID 6561901, 16 pages, 2018.
- [15] C. Lebosse, P. Renaud, B. Bayle, and M. de Mathelin, “Modeling and evaluation of low-cost force sensors,” *IEEE Transactions on Robotics*, vol. 27, no. 4, pp. 815–822, 2011.
- [16] O. Kanoun, C. Müller, A. Benchirouf et al., “Flexible carbon nanotube films for high performance strain sensors,” *Sensors*, vol. 14, no. 6, pp. 10042–10071, 2014.
- [17] A. Sanli, C. Müller, O. Kanoun, C. Elibol, and M. F.-X. Wagner, “Piezoresistive characterization of multi-walled carbon nanotube-epoxy based flexible strain sensitive films by impedance spectroscopy,” *Composites Science and Technology*, vol. 122, pp. 18–26, 2016.
- [18] G. Canavese, S. Stassi, C. Fallauto et al., “Piezoresistive flexible composite for robotic tactile applications,” *Sensors and Actuators A: Physical*, vol. 208, pp. 1–9, 2014.
- [19] P. Silva, P. Pinto, O. Postolache, and J. Dias, “Tactile sensors for robotic applications,” *Measurement*, vol. 46, no. 3, pp. 1257–1271, 2013.
- [20] M. Tiwana, S. Redmond, and N. Lovell, “A review of tactile sensing technologies with applications in biomedical engineering,” *Sensors and Actuators A: Physical*, vol. 179, pp. 17–31, 2012.
- [21] R. Dahiya, G. Metta, M. Valle, and G. Sandini, “Tactile sensing from humans to humanoids,” *IEEE Transactions on Robotics*, vol. 26, no. 1, pp. 1–20, 2010.
- [22] S. Dempsey, M. Szablewski, and D. Atkinson, “Tactile sensing in human-computer interfaces: the inclusion of pressure sensitivity as a third dimension of user input,” *Sensors and Actuators A: Physical*, vol. 232, pp. 229–250, 2015.
- [23] N. Behera, J. Duan, W. Jin, and S. Kitagawa, “The chemistry and applications of flexible porous coordination polymers,” *EnergyChem*, vol. 3, no. 6, article 100067, 2021.
- [24] S. Zheng, Q. Li, H. Xue, H. Pang, and Q. Xu, “A highly alkaline-stable metal oxide@metal-organic framework composite for high-performance electrochemical energy storage,” *National Science Review*, vol. 7, no. 2, pp. 305–314, 2020.
- [25] C. Liu, Y. Bai, W. Li, F. Yang, G. Zhang, and H. Pang, “In situ growth of three-dimensional mxene/metal-organic framework composites for high-performance supercapacitors,” *Angewandte Chemie International Edition*, vol. 61, no. 11, article e202116282, 2022.
- [26] C. Lebosse, B. Bayle, M. de Mathelin, and P. Renaud, “Nonlinear modeling of low cost force sensors,” in *2008 IEEE*

- International Conference on Robotics and Automation*, pp. 3437–3442, Pasadena, CA, USA, May 2008.
- [27] L. Paredes-Madrid, A. Matute, and C. Palacio, “Understanding the effect of sourcing voltage and driving circuit in the repeatability of measurements in force sensing resistors (fsrs),” *Measurement Science and Technology*, vol. 30, no. 11, article 115101, 2019.
- [28] L. Paredes-Madrid, J. Fonseca, A. Matute, E. I. G. Velásquez, and C. A. Palacio, “Enhancing the repeatability of pressure-mapping insoles by choosing an appropriate driving circuit and sourcing voltage,” in *2018 7th IEEE International Conference on Biomedical Robotics and Biomechanics (Biorob)*, pp. 1193–1198, Enschede, NL, Aug 2018.
- [29] L. Lin, S. Liu, Q. Zhang et al., “Towards tunable sensitivity of electrical property to strain for conductive polymer composites based on thermoplastic elastomer,” *ACS Applied Materials & Interfaces*, vol. 5, no. 12, pp. 5815–5824, 2013.
- [30] Y. Zheng, Y. Li, K. Dai et al., “Conductive thermoplastic polyurethane composites with tunable piezoresistivity by modulating the filler dimensionality for flexible strain sensors,” *Composites Part A: Applied Science and Manufacturing*, vol. 101, pp. 41–49, 2017.
- [31] D. Altuve, L. Paredes-Madrid, and G. Fernandez, “Rough surface modeling of PDMS polymer through fractal dimensions,” 2018.
- [32] K. Samridhi and P. A. Alvi, “Finite element analysis of polysilicon based mems temperature-pressure sensor,” *Materials Today: Proceedings*, vol. 27, pp. 280–283, 2020.
- [33] A. Hossain and A. Mian, “Four-terminal square piezoresistive sensors for mems pressure sensing,” *Journal of Sensors*, vol. 2017, Article ID 6954875, 11 pages, 2017.
- [34] J. O. Dennis, A. A. S. Rabih, M. H. Md Khir, M. G. A. Ahmed, and A. Y. Ahmed, “Modeling and finite element analysis simulation of MEMS based acetone vapor sensor for noninvasive screening of diabetes,” *Journal of Sensors*, vol. 2016, Article ID 9563938, 14 pages, 2016.
- [35] A. Matute, L. Paredes-Madrid, E. Gutierrez, and C. A. P. Vargas, “Characterization of drift and hysteresis errors in force sensing resistors considering their piezocapacitive effect,” in *2017 IEEE Sensors*, pp. 1–3, Glasgow, UK, Oct 2017.
- [36] F. Mainardi and G. Spada, “Creep, relaxation and viscosity properties for basic fractional models in rheology,” *The European Physical Journal Special Topics*, vol. 193, no. 1, pp. 133–160, 2011.
- [37] Y. M. Poplavko, “Chapter 2 - mechanical properties of solids,” in *Electronic Materials*, pp. 71–93, Elsevier, Amsterdam, Netherlands, 2019.
- [38] M. Martinez and A. Artemev, “A novel approach to a piezoelectric sensing element,” *Journal of Sensors*, vol. 2010, Article ID 816068, 5 pages, 2010.
- [39] P. Hashemi, M. Mehranpour, and I. Ghasemi, “Fabrication of a strain sensor based on polymer/silver nanowires nanocomposite for medical applications: Siloxane based versus urethane based nanocomposites,” *Polymer Composites*, vol. 42, no. 3, pp. 1440–1450, 2021.
- [40] J. Britton, K. Krukiewicz, M. Chandran et al., “A flexible strain-responsive sensor fabricated from a biocompatible electronic ink via an additive-manufacturing process,” *Materials & Design*, vol. 206, article 109700, 2021.
- [41] B. J. van Wees, H. van Houten, C. W. J. Beenakker et al., “Quantized conductance of point contacts in a two-dimensional electron gas,” *Physical Review Letters*, vol. 60, no. 9, pp. 848–850, 1988.
- [42] D. Wharam, T. Thornton, R. Newbury et al., “One-dimensional transport and the quantisation of the ballistic resistance,” *Journal of Physics C: Solid State Physics*, vol. 21, no. 8, pp. L209–L214, 1988.
- [43] G. Timp, “Chapter 3: when does a wire become an electron waveguide,” *Semicon. Semimetals*, vol. 35, pp. 113–190, 1992.